The treatment of singularities associated with a dislocation segment with applications

Abu Bakar Siddique and Tariq A. Khraishi*

Mechanical Engineering Department,
University of New Mexico,
Albuquerque, New Mexico, USA
Fax: +1-505-277-1571
Email: abakarsiddique@unm.edu
Email: khraishi@unm.edu
*Corresponding author

Abstract: Quantification of the stress field around dislocations is important in dislocation theory and can have profound effect on computations involving dislocations such as in discrete dislocation dynamics (DDD) simulations. In this paper, the original work by Devincre (1995) on the stress field of a linear dislocation segment is carefully studied and based on three regions of space, a physics-based algorithm is presented to treat any singularity, weak or strong, associated with the self-stress of the segment. The paper shows several utilisations of this method. Two of these utilisations concern the 'collocation-point' method for capturing free-surface effects on dislocation forces and movement. In one, an on-the-fly mesh was utilised, and in the other an unstructured mesh was utilised. Results were validated where appropriate and both static and dynamic implementations are presented.

Keywords: dislocation dynamics; free surfaces; collocation-point method; flow stress; image stresses.

Reference to this paper should be made as follows: Siddique, A.B. and Khraishi, T.A. (2021) 'The treatment of singularities associated with a dislocation segment with applications', *Int. J. Theoretical and Applied Multiscale Mechanics*, Vol. 3, No. 4, pp.287–312.

Biographical notes: Abu Bakar Siddique received his MS in Mechanical Engineering from the University of New Mexico, Albuquerque, New Mexico, in 2016. He is currently a PhD student in Mechanical Engineering at the University of New Mexico. His research mainly focuses on plasticity modelling. He modelled the surface correction terms for static dislocation problems near any free surfaces and successfully implemented his model to a discrete dislocation dynamics code. He also modelled dislocations interaction in a multipole configuration and explored the hardening/softening effects from the interactions. His research work was done in collaboration with the Sandia National Labs. He has published his work in several peer-reviewed journals.

Tariq A. Khraishi is a Professor of Mechanical Engineering at the University of New Mexico. He obtained his PhD from the School of Mechanical and Materials Engineering at Washington State University, in 2000. His research work is in the general areas of mechanics and materials science. In particular, he has performed modelling, theoretical and/or experimental research in biomechanics, dislocation dynamics, eigenstrain theory/modelling, fracture mechanics, nano structures, irradiation damage, void growth/interaction in

superplasticity, and stresses in thin films. He has received many awards for exemplary research and teaching. He has published over 120 refereed publications including chapter contributions and books.

1 Introduction

Dislocation theory is a branch of materials science that is focused on the carriers of plasticity in crystalline solids or metals. Understanding how and why dislocation moves and interact between themselves and other micro-constituents will enable understanding of the plasticity phenomenon in crystals (Hirth and Lothe, 1982; Weeterman and Weeterman, 1992; Hull and Bacon, 2011). With many developments in dislocation theory, which were followed after by experimental evidence, the stage was set for developing plasticity models that take dislocations directly into account. Some of these models are based on dislocation densities as a field variable, i.e., a continuum approach (Acharya, 2003; Schulz et al., 2014; Zhu and Xiang, 2015), and some are based on modelling 3D discrete dislocations and their dynamics (Kubin et al., 1992; Zbib et al., 1998; Khraishi and Zbib, 2001; Khraishi et al., 2004; Leger et al., 2004; Devincre et al., 2008).

The latter approach for modelling or simulating the dynamics of discrete dislocations was made possible by the ability to discretise a curved dislocation line into segments [similar to the finite element (FE) method which discretises space into finite elements of different shapes]. Hirth and Lothe (1982) developed the stress field associated with a linear dislocation segment using a segment-attached coordinate system, where the z-axis coincides with the segment line. Devincre (1995), building on the work of de Wit (1967), developed expressions for the stress field of a linear dislocation segment based on an arbitrary located coordinate system. Cai et al. (2006) developed the expression for the stresses of a dislocation segment using nonlinear elasticity by spreading the Burgers vector of the line to avoid the common singularity. The result of this is more complex than the prior works, but it reduces to these prior works with no spreading (or zero spreading). Ghoniem and Sun (1999) described a dislocation curve using general topological functions. All of the above works are within the realm of isotropic elasticity and apply to an infinite medium. The line singularity was also treated in the work of Jamond et al. (2016) using the discrete-continuous model (DCM) for the simulation of 3D dislocation dynamics (DD) which is based on a coupling between a DD code and a FE code through eigenstrain theory.

The current paper focuses on the leading work of Devincre (1995) by closely looking at the spatial regions around a linear dislocation segment and properly treating the segment stresses in order to avoid singularities in the solution. This enables the regularisation of the stress field. The space around the segment is divided into three distinct regions discussed in Section 2. By correctly placing a field point in the right region, the segment stress can then be calculated correctly or appropriately while avoiding singular calculations. Such regularisation is important in DD simulations as the time-dependent solution can blow up or become unbounded if a field point lies in a singularity zone. To illustrate the method, including the accompanying algorithm

developed here, a couple of applications are presented in Section 3. The examples revolve around the use of the distributed dislocation method, which can be used to solve crack problems (Hills et al., 1996; Khraishi and Demir, 2003; Demir and Khraishi, 2005), for solving the stress field of dislocations near a flat free surface (Khraishi et al., 2001; Khraishi and Zbib, 2002; Yan et al., 2004; Siddique and Khraishi, 2020, 2021a) or near a curved surface (Siddique and Khraishi, 2021b). These methods are 'collocation point' methods where the zero traction physical boundary condition is enforced at a set of different surface points instead of an infinite number of them. These collocation points represent the centres of elements on a surface mesh whereby each element is represented by a multi-polygonal dislocation loop (which by itself is a self-equilibrated source of stress in the material). By figuring out the Burgers vectors of these surface fictitious/mathematical dislocation loops, the problem is then solved and the stress field at any sub-surface field point is the sum of the stress fields of surface loops plus the stress fields of the sub-surface dislocations.

The latest of Siddique and Khraishi (2020) utilised a surface mesh of rectangular/square elements with each element composed of four linear dislocation segments whereby the whole computations are made in reference to an arbitrary-oriented global coordinate system. For this referenced work, the selection of collocation points had to be chosen carefully so as not to lie in the singularity zone, even the extended singularity zone, of any of the elements' segments. More specifically, this structured surface mesh of elements had to look like a standard finite-element mesh in the sense that each element node has to be the node for four dislocation segments. In other words, a node for a dislocation segment cannot be a no node for an element. This severely restricts the meshing type used for the surface which can have ramifications on things like solution time for a static or dynamic problem. Of course, treating free surface problems can be attempted analytically (Yoffe, 1961; Chou, 1963; Baštecká, 1964; Bacon and Groves, 1970; Groves and Bacon, 1970; Maurissen and Capella, 1974b, 1974a; Comninou and Dundurs, 1975; Lothe et al., 1982; Jing et al., 2009; Li and Khraishi, 2021; Li et al., 2021) but such treatment is severely restricted in scope and breadth since it has to be specific to a certain configuration of the domain and of the dislocation near the surface.

In this current work, we utilise the newly proposed non-singular stress field associated with a dislocation segment in application to new surface meshing of fictitious/mathematical dislocation loops. Specifically, we look at an irregular square/rectangular mesh, termed here 'on-the-fly mesh' and also at an unstructured (or random) triangular-element mesh. Both of these meshes, albeit having their own advantages over a structured rectangular-element/square-element mesh, can run into singularity issues but are treated here with the newly developed method/algorithm. The 'on-the-fly mesh' is illustrated here for static dislocation problems and the unstructured triangular mesh is illustrated here for dynamic dislocation problems.

In addition to the above, this current work looks closely at the extent of the dislocation core radius or size. There are different estimates in the literature for the radius of the core, r_c (Hirth and Lothe, 1982; Meyers and Chawla, 2009; Hull and Bacon, 2011). Based on the regularisation of the segment stress introduced here, a rationale for the quantification of r_c is provided as well.

2 Methods

As mentioned above, this work builds on the work of Devincre (1995) for the stress field of a linear dislocation segment in a linear-elastic isotropic infinite medium. For a segment *AB* of a dislocation line, shown in Figure 1, the stresses at a field point *P*(*x*, *y*, *z*) according to this last reference are provided with respect to a generally-oriented global coordinate systems centred at *O* by:

$$\sigma_{\alpha\beta}^{AB}(\vec{r}) = \left(\sigma_{\alpha\beta}^{AB}\right)_{\vec{r}'=\overrightarrow{OB}} - \left(\sigma_{\alpha\beta}^{AB}\right)_{\vec{r}'=\overrightarrow{OA}} \tag{1}$$

and $\sigma_{\alpha\beta}^{AB}$ is described as:

$$\begin{aligned}\sigma_{\alpha\beta}^{AB} = \frac{\mu}{\pi Y^2}\Bigg[&[\vec{b}\vec{Y}\vec{t}]_{\alpha\beta}^{s} - \frac{1}{(1-\nu)}[\vec{b}\vec{t}\vec{Y}]_{\alpha\beta}^{s} \\ &-\frac{(\vec{b},\vec{Y},\vec{t})}{2(1-\nu)}\left[\delta_{\alpha\beta} + t_\alpha t_\beta + \frac{2}{Y^2}\left[\rho_\alpha Y_\beta + Y_\alpha \rho_\beta + \frac{L}{R}Y_\alpha Y_\beta\right]\right]\Bigg]\end{aligned} \tag{2}$$

where μ is the isotropic material shear modulus (also given by *G* in literature), ν is the Poisson's ratio and

$$\vec{R} = \vec{r} - \vec{r}' \tag{3.1}$$

$$L = \vec{R}\cdot\vec{t} \tag{3.2}$$

$$\vec{\rho} = \vec{R} - L\vec{t} \tag{3.3}$$

$$\vec{Y} = \vec{R} + R\vec{t} \tag{3.4}$$

Here, $(\vec{a},\vec{b},\vec{c})$ is called a 'scalar triple product' and is given by:

$$\left(\vec{a},\vec{b},\vec{c}\right) = \left(\vec{a}\times\vec{b}\right)\cdot\vec{c} \tag{4}$$

and $[\vec{a}\vec{b}\vec{c}]_{\alpha\beta}^{s}$ is called a 'symmetric tensor operator' and is given by:

$$[\vec{a}\vec{b}\vec{c}]_{\alpha\beta}^{s} = \frac{1}{2}\left(\left(\vec{a}\times\vec{b}\right)_\alpha c_\beta + \left(\vec{a}\times\vec{b}\right)_\beta c_\alpha\right) \tag{5}$$

Here, r_c is a cut-off radius delineating the core region of the dislocation (also called core radius for simplicity) where the self-stress of the dislocation shoots up to infinity under the use of linear-isotropic elasticity. The reason for this singular behaviour is that the treatments of a dislocation viewed it as line defect experiencing a sudden displacement shift equal to the Burgers vector $\mathbf{b} = \vec{b} = (b_x, b_y, b_z)$. The magnitude of the Burgers vector is indicated here as *b*. This discontinuous shift in the displacement field of the dislocation causes a singularity in the strain field, which is carried to the stress field via Hooke's law. The magnitude of r_c has been chosen differently in the literature, i.e., it has not been agreed upon or is a subject of debate. For example, Hirth and Lothe (1982) took r_c as 1*b*, Hull and Bacon (2011) took it as 1*b*–4*b*, Meyers and Chawla (2009) took it as

5*b*, and so forth. One of the things provided or contributed by this work, as alluded to earlier, is an attempt at quantifying r_c in a fundamental way as seen below.

Figure 1 A dislocation segment *AB* with three identifiable regions in space (see online version for colours)

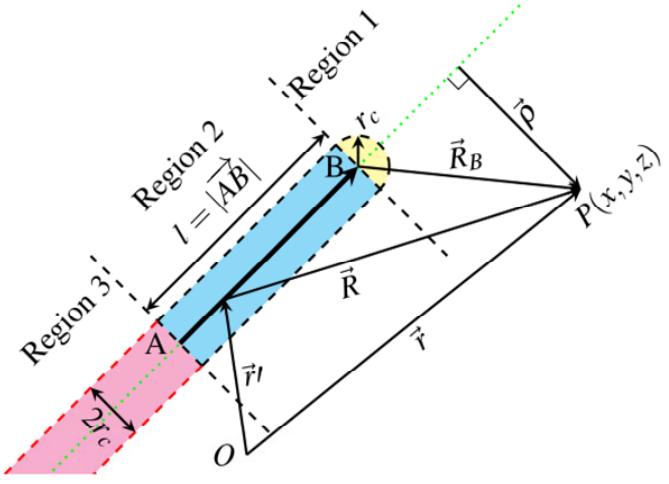

Notes: The line sense unit vector $\vec{t}$ points from *A* to *B*. dislocation segment length:

$$l = |\vec{r}_B - \vec{r}_A| = |\overrightarrow{AB}|.$$

To better understand the behaviour of stress around segment *AB*, contour plotting is used to give an overall look of stress distribution. Figure 2 shows contour plotting for two exemplary stress components σ_{11} and σ_{12}. Other stress components behave similarly. Taking a close look at Figure 2, it is clear that stress values shoot up in value (indefinitely) immediately around the segment (labelled Region 2 in Figure 1) and behind the segment (from point *A* opposite to the line sense, which is labelled Region 3 in Figure 1). However, one would expect the stress around the mid-plane intersecting the segment centre to be symmetric (i.e., Region 3 the mirror opposite of Region 1) or at least anti-symmetric which is not the case. This behaviour is due to what equation (1) stands for. In equation (1), the stress from a half dislocation line extending from –∞ to point *B* is subtracted from the stress from a half dislocation line extending from –∞ to point *A*. This subtraction yields the stress of a dislocation line segment *AB*. Due to this subtraction process, it is recognised then that the stress at the dislocation line in Region 2 is strongly singular due to the issues discussed prior. It is also recognised that the stress at the dislocation line in Region 3 is expected to be weakly singular and right at the line itself due to the effect of the subtraction. Moreover, the stress in Region 1 seems to be (for the most part at least) non-singular and well behaving in values/distribution. In fact, in Figure 2, a cut-off radius of 0.05*b* was utilised in Regions 2 and 3 to be able to do the plot, otherwise the stress would shoot to infinity there. Even with this implemented cut-off, the stress values are significant compared to the shear modulus.

Although the above was a visual investigation of the stress behaviour, especially singularity behaviour, of the dislocation segment, one can carefully examine equation (2), which feeds into equation (1), to see where the singularity exactly emanates from.

Figure 2 Contour plots around a linear dislocation segment lying in the *xy*-plane, (a) σ_{11} (b) σ_{12} (see online version for colours)

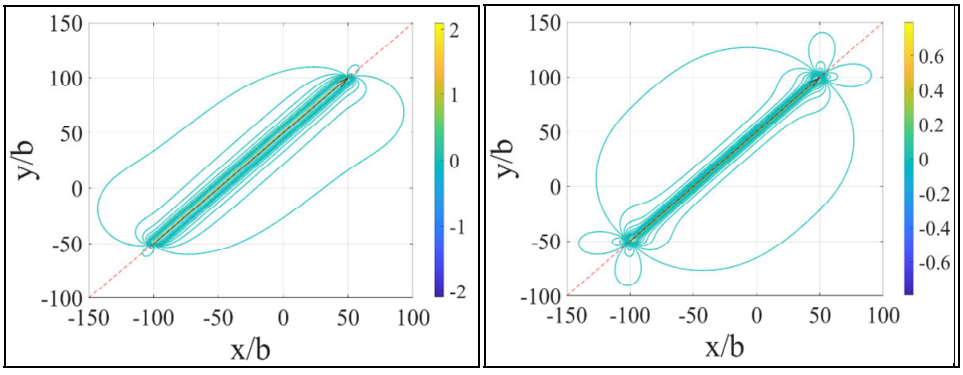

(a) (b)

Notes: These are made before implementing the algorithm in this paper (in the contour plots, points with $r_c < 0.05$ were ignored). The coordinates of point *a* are (–100, –50, 0) and for point *b* are (50, 100, 0). Here, the burgers vector = (1/√3, 1/√3, 1/√3) for simplicity. Here, $\mu = G = 1$ and $\nu = 0.33$.

Consider point *B* of dislocation segment *AB*. From equation (3.2), one can write:

$$L_B = (\vec{r}_P - \vec{r}_B)\cdot\vec{t} = \vec{R}_B\cdot\vec{t} \tag{6}$$

For any field point *P*, $\vec{\rho}$ is given by [equation (3.3)]:

$$\vec{\rho} = \vec{R}_B - L_B\vec{t} \tag{7}$$

Examining equation (2), it becomes unbounded if and only if either *Y* or R approaches zero. From the definition of $\vec{Y}$:

$$\vec{Y} = \vec{\rho} + L\vec{t} + \left|\vec{\rho} + L\vec{t}\right|\vec{t} \tag{8}$$

$Y = 0$ when, $\rho = 0$ and $L_B \leq 0$. This can happen in Regions 2 and 3 only and not in Region 1. In Region 1 therefore, there is no worry about singular stress behaviour. However, special attention needs to be paid to the domed region around point *B* (see Figure 1). In the following is an algorithm that checks against ρ approaching zero and then adjusts the stress calculation procedure accordingly.

Algorithm

1 Calculate the quantity ρ per above. If $\rho \geq r_c$, no additional treatment is needed since point $P(x, y, z)$ lies outside the core region of the dislocation and therefore the stress equations [equations (1) and (2)] are valid as is.

2 If $\rho < r_c$:

   a If $L_B > 0$ [point $P(x, y, z)$ lies in Region 1 (yellow) in Figure 1]:

      1 If $R_B \geq r_c$, then no additional treatment is required (since $Y > r_c$).

      2 If $R_B < r_c$, then the field point is within the domed area atop of point *B*. In this case, point *P* location has to be adjusted away from the dislocation line such that $\vec{\rho}$ is scaled up in magnitude to match r_c as shown in Figure 3. Once $\vec{\rho}'$ (the new $\vec{\rho}$) is

calculated $\left(\text{via } \vec{\rho}' = \vec{\rho} \times \frac{r_c}{\rho}\right)$, a new adjusted location for point P (point P') can be determined [using equation (3.3), i.e., $\vec{R} = \vec{\rho} + L\vec{t}$]. Now, stress calculations can be performed at this new location.

b If $L_B \leq 0$ and $|L_B| \leq 1$ [point $P(x, y, z)$ lies in Region 2 (cyan) in Figure 1]:

To find the stress at this point, one needs to do a linear interpolation between 0 and $\sigma_{ij}^{\max}$. More on this linear interpolation is given below in detail.

c If $L_B \leq 0$ and $|L_B| > 1$ [point $P(x, y, z)$ lies in Region 3 (magenta) in Figure 1]:

1 Reverse $\vec{t}$ and calculate segment stress and then multiply the obtained stress value by (–1) or a negative sign. In other words, calculate the stress for a directed segment from B to A instead of from A to B.

2 Alternate to 2.c.1 above, if $\rho \geq \varepsilon$, where ε could be as small as 10^{-10} or almost the computer machine zero, then one can proceed with normal stress calculations for the segment using equations (1) and (2). This is possible due to the weak singular behaviour in Region 3.

The algorithm is shown in Figure 4 as a flowchart.

Figure 3 Recommended location of P when, (a) $\boldsymbol{L}_B > 0$ and $\boldsymbol{R}_B < r_c$ (b) Case 2.b in the algorithm (see online version for colours)

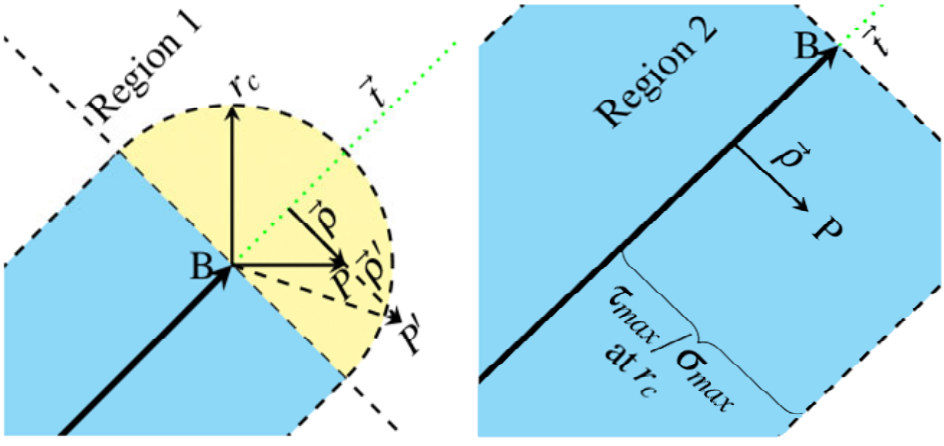

(a) (b)

Note: (a) Region 1 and (b) Region 2.

For Case 2.b above, the steps for linear interpolation are as follows [refer to Figure 3(b)]:

1 First, find the value of ρ for point P using equation (3.3).

2 Multiply $\vec{\rho}$ with the quantity $\frac{r_c}{\rho}$, i.e., $\vec{\rho}' = \vec{\rho} \times \frac{r_c}{\rho}$ which extends to the core surface.

3 Find a new $\vec{R}_B$ value as such: $\vec{R}_B{}' = \vec{\rho}' + L_B\vec{t}$. From this, find a new $\vec{Y}$ value [equation 3.4].

4 Substitute back $\vec{\rho}'$ and $\vec{R}_B{}'$ (and the new $\vec{Y}$ value) into equation (2) and then equation (1) to find the limiting value of $\sigma_{ij}^{\max}$.

5 Now, the interpolated value of the stress is given by: $\sigma_{ij}(P) = \frac{\rho}{r_c} \times \sigma_{ij}^{\max}$.

Figure 4 Flowchart of the algorithm (see online version for colours)

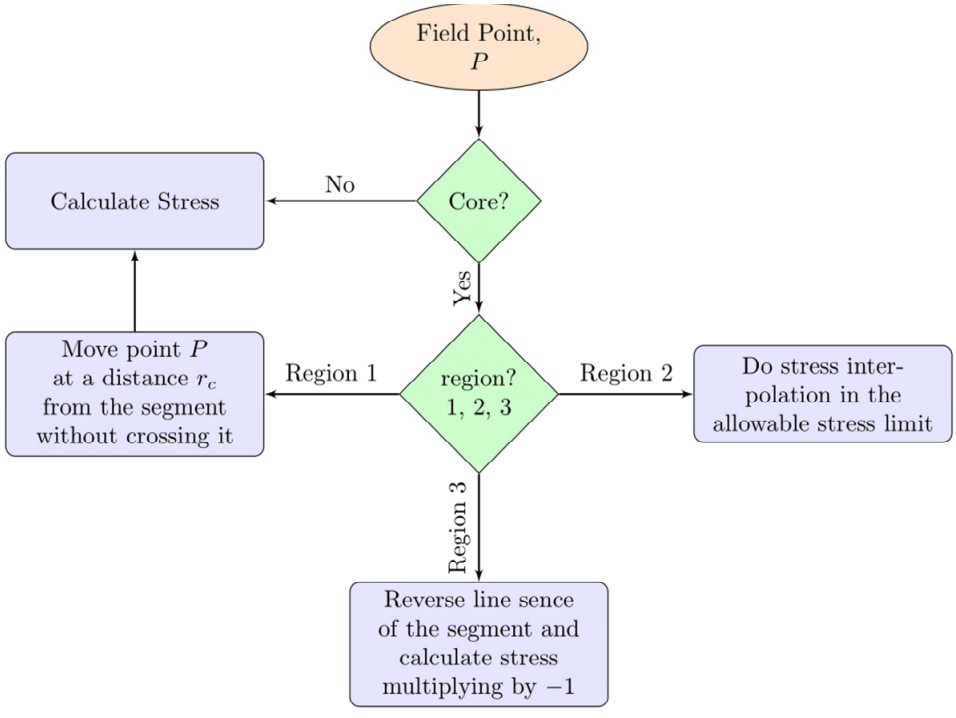

Lastly, it was mentioned above about the strong singularity occurring in Region 2. If one considers any plane containing the dislocation line segment and then plots any of the stress components σ_{ij} along a coordinate ξ perpendicular to the line, one gets a spatial behaviour as shown in Figure 5. In the schematic figure, the stress shoots to infinity as the dislocation line is approached. However, according to theory, stress must have a maximum theoretical value in a material that cannot be exceeded. According to Hull and Bacon (2011), the maximum shear stress (indicated by the symbol taw or τ) is given by $\tau_{\max} = \frac{G}{2\pi}$. In Meyers and Chawla (2009), the maximum shear stress is given by $\tau_{\max} = \frac{G}{5.1}$. However, according to Hull and Bacon (2011), a more realistic value for the maximum shear stress is given by $\tau_{\max} = \frac{G}{30}$. In addition, elementary mechanics of materials theory dictates that for the simple case of uniaxial stress, the normal stress σ is double the shear stress τ in value, i.e., $\sigma_{\max} = 2\tau_{\max}$. Based on these maximum values for

the different stress components, one can arrive at a calculated value for r_c per this figure. Figure 5 also shows that within the core region in Region 2, the stress could be interpolated for values as the interpolation (linear interpolation is the most logical in this case) passes through zero at the dislocation line (i.e., the core centre) due to the change in sign for the stress shown in Figure 5. The zero value at the dislocation centre also makes physical sense since the dislocation cannot stress its own self. The exact steps to perform the interpolation were listed above.

Figure 5 Schematic of stress behaviour around a linear dislocation segment versus a coordinate traversing perpendicular to the segment (in Region 2)

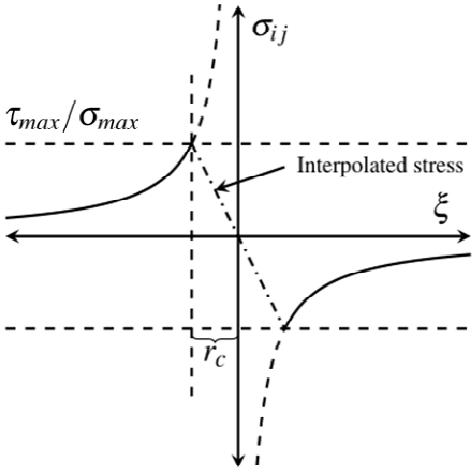

3 Results and discussion

Upon implementation of the algorithm above, one can verify the produced results in several way. For example, let us take a segment AB of length $150\sqrt{2}$ lying in the xy-plane for simplicity. The coordinates of points A and B are $(-100b, -50b, 0)$ and $(50b, 100b, 0)$, respectively. Let us also take a Burgers vector equal to: $\frac{1}{\sqrt{3}}, \frac{1}{\sqrt{3}}, \frac{1}{\sqrt{3}}$ for simplicity. The reason for choosing a Burgers vector with all three components not being zero is to elucidate any possible contributions from these components to the different stress components. Here, $\mu = G = 1$ and $\nu = 0.33$.

Figure 6 shows plots for three stress components (σ_{11}, σ_{12}, σ_{13} and σ_{33}) versus coordinate ξ (expressed, and any coordinate, in units of b) which is perpendicular to the dislocation line and passing through the segment's centre. The reason these components are chosen is that the first one (σ_{11}) is the same plot as σ_{22} and the third (σ_{13}) is the same plot as σ_{23}. In Figure 6, one can notice that all the stress components follow the schematic plot for stress distribution in Figure 5. Per Figure 5, the plots in Figure 6 could be used to find a good estimate for r_c based on the reported values for the maximum shear stress provided in the textbooks of Hull and Bacon (2011) and Meyers and Chawla (2009) textbook (see above). Based on these three estimates for the maximum shear stress value,

Table 1 can be generated and it shows estimates of r_c based on maximum shear stress values (or correspondingly maximum normal stress values from introductory mechanics of materials, see above). Based on the tabulated values, a conservative estimate for the core radius r_c is 2.75b (or ~3b). Notice that this value is between those reported in the literature [for example, Hirth and Lothe (1982) took r_c as 1b, Hull and Bacon (2011) took it as 1b–4b, Meyers and Chawla (2009) took it as 5b, and so forth].

Figure 6 Plots of different stress components, in Region 2, along the ξ direction in an xy-plane containing a dislocation segment and passing through the centre of the segment, (a) σ_{11} (b) σ_{33} (c) σ_{13} (d) σ_{12} (see online version for colours)

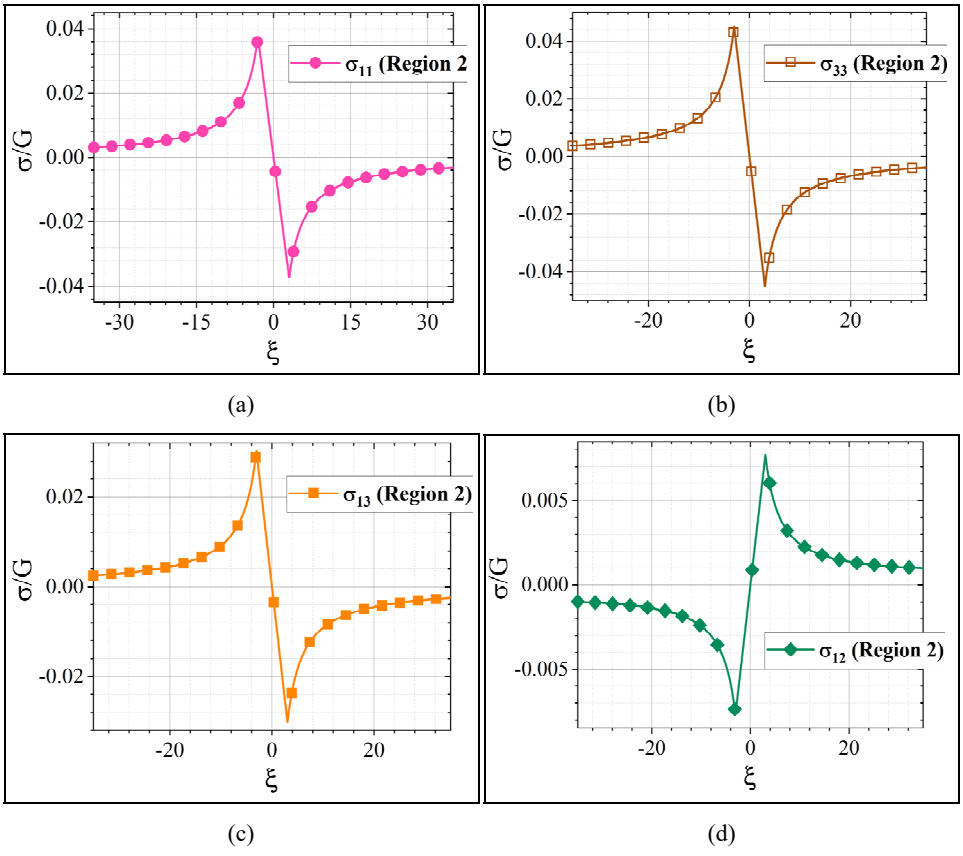

Note: Note that in all these plots, the curve passes through the (0, 0) point.

In addition to Figure 6, one now can do contour plots for the above dislocation segment example which lies in the xy-plane. Now that the above algorithm is implemented, Figure 7 shows contour plots for all the stress components. Note that the plot for σ_{23} is the same as for σ_{13}. The plots are done using $r_c = 3b$ in Region 2. Notice that the stress levels in these contour plots is considerably less than those in Figure 2 since (by employing the above algorithm) the stress levels are either capped in Figure 2 based on theoretical grounds in Region 2 or the weak singularity completely removed/terminated in Region 3. Moreover, notice in these new figures, the perfect symmetry or anti-symmetry alluded to

earlier around the plane perpendicular to the segment at is centre. This is another indication of the success of the above algorithm in attaining the goals of this work.

Figure 7 Contour plots around a linear dislocation segment lying in the *xy*-plane, (a) σ_{11} (b) σ_{22} (c) σ_{33} (d) σ_{23} (e) σ_{13} (f) σ_{12} (see online version for colours)

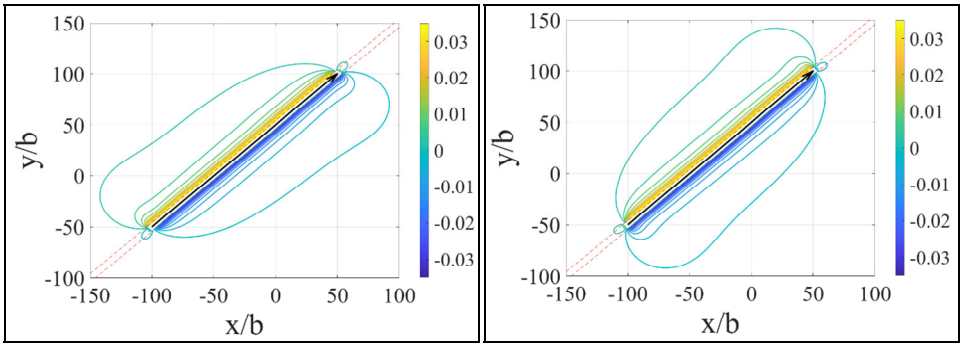

(a) (b)

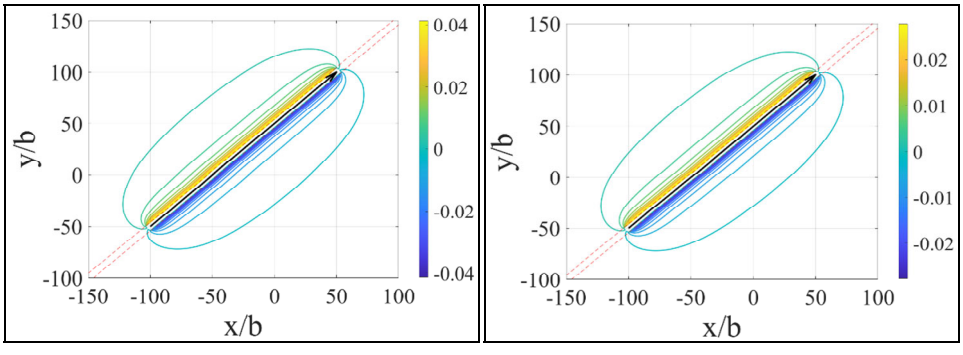

(c) (d)

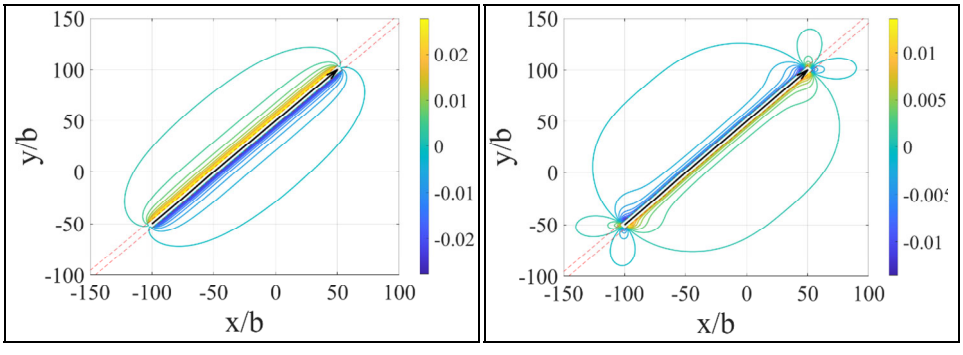

(c) (d)

Notes: These are made after implementing the algorithm in this paper. Applying the algorithm for the parameters: $r_c = 3b$, the coordinates of point A are (–100, –50, 0) and for point B are (50, 100, 0). Here, the Burgers vector = $\left(\frac{1}{\sqrt{3}}, \frac{1}{\sqrt{3}}, \frac{1}{\sqrt{3}}\right)$ for simplicity. Here, $\mu = G = 1$ and $\nu = 0.33$.

Figure 8 Line plots of stress showing the disappearance of the singularity in Region 3 with the application of the method in this paper, (a) σ_{11} (b) σ_{22} (c) σ_{33} (d) σ_{23} (e) σ_{13} (f) σ_{12} (see online version for colours)

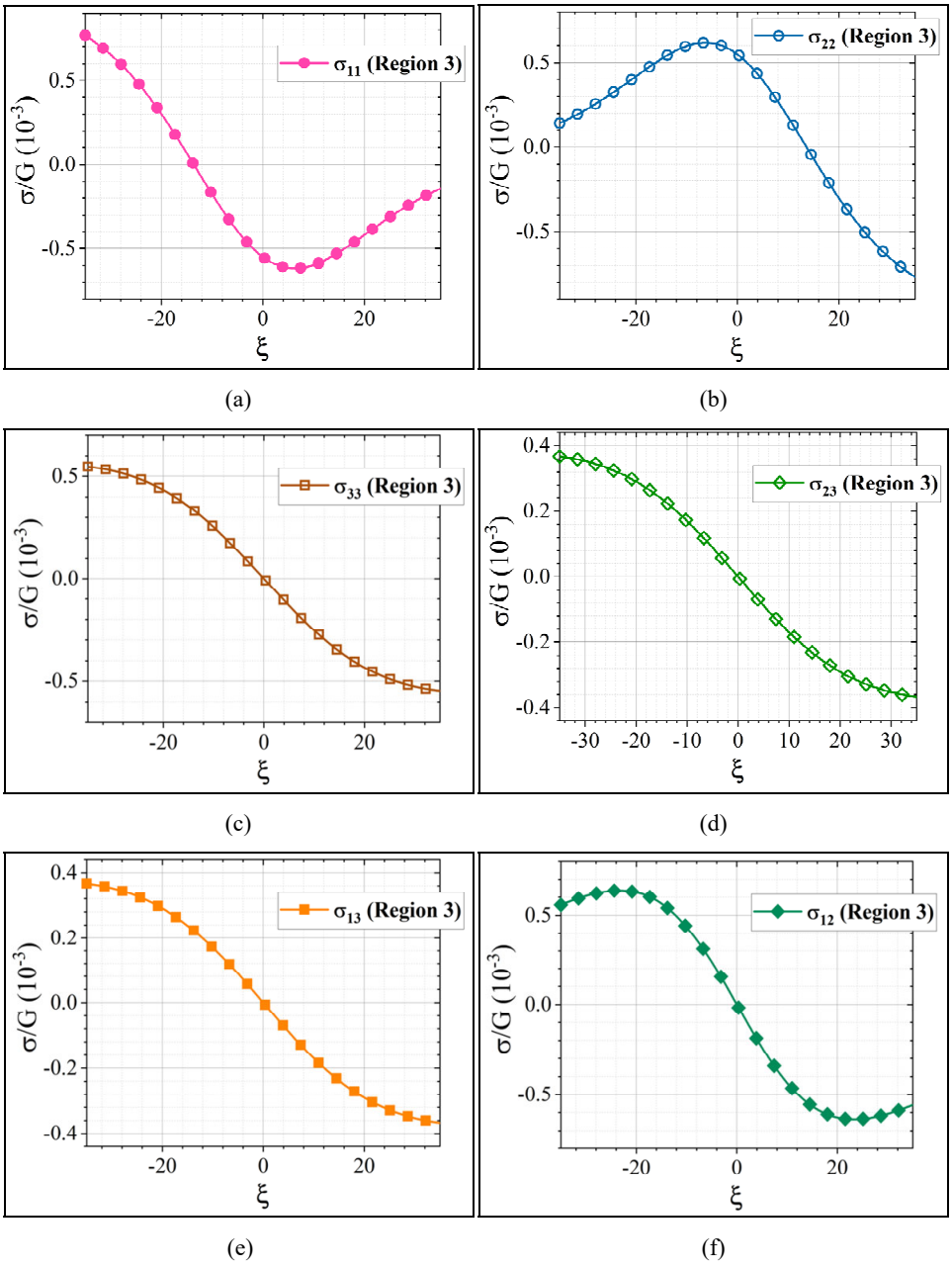

Another verification of the efficacy of the employed procedure or algorithm is shown in Figure 8 which shows line plots for the different stress components, all for Region 3. All of these line plots are for the segment mentioned above which lies in the *xy*-plane (with *b* equal to unity here for simplicity). Here again, and for this particular segment, the plot σ_{23}

is the same as for σ_{13}. The ξ parameter here is also normal to the dislocation line and lying in the *xy*-plane as before but it is perpendicular to the line (or really the line extension) in Region 3 and not in Region 2 like the plots in Figure 6. For completeness sake, the ξ line was behind point *A* by 50*b* although the exact distance behind will only influence the values on the plotted stress components but not the shape of the curve. It is clear in Figure 8, that by applying the above algorithm, that there are no singularities, not even the weak singularity, expected to be found in Region 3. Hence, the above method is working well again for eliminating the singularities associated with the core region of the dislocation segment. Notice that in Region 3, one can have a similar result to Figure 8 by making $r_c \rightarrow \varepsilon$ and not just by flipping the line sense. This was pointed out in the procedure above.

Table 1 Calculation of r_c, in terms of *b*, based on the maximum shear stress or normal stress values using three different sources for the maximum value

	r_c *based on:* $\tau_{\max} = \frac{G}{2\pi}$	r_c *based on:* $\tau_{\max} = \frac{G}{5.1}$	r_c *based on:* $\tau_{\max} = \frac{G}{30}$
σ_{11}	0.3620	0.2942	1.7423
σ_{22}	0.3620	0.2942	1.7423
σ_{33}	0.4299	0.3394	2.0478
σ_{23}	0.5770	0.4639	2.7492
σ_{13}	0.5770	0.4639	2.7492
σ_{12}	0.2828	0.2263	1.3463

In addition to the above examples on the efficacy of the method or algorithm of this paper, another application of the method is presented here. In dislocation problems, both static and dynamic, the issue of dealing with the presence of a free surface in the computational domain frequently presents itself. Although there are different ways to deal with existence of free surfaces that can be found in Canova and Fivel (1999), Hartmaier et al. (1999), El-Azab (2000) and Deng et al. (2008), the focus here is on works that utilised the 'collocation point method' to ensure that such surface is free from stress traction (Khraishi et al., 2001; Khraishi and Zbib, 2002; Yan et al., 2004; Siddique and Khraishi, 2020). The problem arises because analytical solutions for dislocation segments are provided [as in equations (1) and (2) above, Hirth and Lothe (1982) or Cai et al. (2006)] for infinite mediums. Such analytical solutions are the basis for discrete dislocation dynamics (DDD) simulations alluded to earlier (Zbib et al., 1998; Khraishi and Zbib, 2001; Khraishi et al., 2004; Leger et al., 2004). However, such DDD simulations are implemented in a finite or confined three-dimensional space or computational domain. When this domain contains free surfaces, additional stress terms (generally referred to historically as 'image stresses') are needed to augment or complement the analytical dislocation segment solutions in order for the zero stress-traction condition to be met, even if partially, on the free surface. In the collocation point method, the zero traction condition is enforced on a collection of *N* surface points, called collocation points. As $N \rightarrow$ infinity, the solution approaches any analytical solution (if one existed). In the collocation point methods presented in Khraishi et al. (2001), Khraishi and Zbib (2002), Yan et al. (2004) and Siddique and Khraishi (2020), the free surface is meshed by a contiguous uniform mesh or grid [see Figure 9(a)], resulting in rectangular/square elements all of equal size, the centre of each such element is a

collocation point. Moreover, the extra 'image stresses' at any crystal field point beneath the planar free surface come from the fact that each surface element in the mesh/grid stands for a generally-prismatic dislocation loop whose Burgers vector components are yet to be determined. The reason for choosing the elements as dislocation loops (which are fictitious or mathematical dislocation loops and not real or crystal ones) is two folds:

a Each such dislocation loop represents a self-equilibrated source of stress in the calculations and hence employing such loops does not disturb the spatial equilibrium or even compatibility in the computational domain.

b Such dislocation loops can provide the extra or complementary stresses representing the 'image stresses' mentioned above.

Figure 9 Free surfaces (a) regular mesh and (b) on-the-fly mesh meshed by regular or irregular meshes with the dots representing collocation points

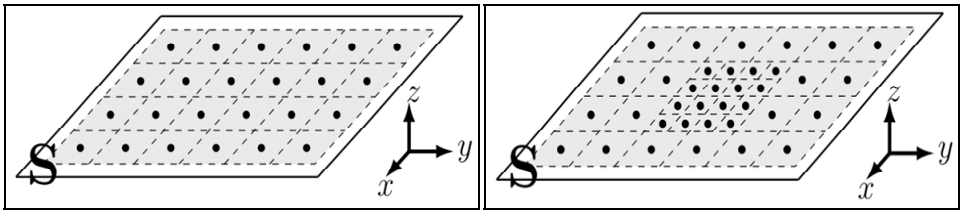

(a) (b)

Note: Dislocations lie beneath the surface in the material.

The problem of such mesh-based collocation method boils down to finding the Burgers vector components (b_x, b_y, b_z) of each loop on the surface. The way to find these Burgers vector components is equations that annul the traction $\vec{T}$ ($\vec{T} = \boldsymbol{\sigma}\vec{n}$, where $\boldsymbol{\sigma}$ is the stress state and $\vec{n}$ is a unit normal vector) at each of the N collocation points. For Figure 9(a), and using elementary continuum mechanics (Khraishi and Shen, 2011), the zero traction condition on the collocation points translates to enforcing $\sigma_{zx} = \sigma_{zy} = \sigma_{zz} = 0$ on each such point. Mathematically, the problem is formulated as such:

$$\sum_{j=1}^{N} \sigma_{xz}^{j\to i} = -\sigma_{xz}^{AB\to i}, \qquad i = 1, 2, \ldots, N \tag{9.1}$$

$$\sum_{j=1}^{N} \sigma_{yz}^{j\to i} = -\sigma_{yz}^{AB\to i}, \qquad i = 1, 2, \ldots, N \tag{9.2}$$

$$\sum_{j=1}^{N} \sigma_{zz}^{j\to i} = -\sigma_{zz}^{AB\to i}, \qquad i = 1, 2, \ldots, N \tag{9.3}$$

where $\sigma_{\alpha\beta}^{j\to i}$ is the $\alpha\beta$ stress component of loop j evaluated or calculated at collocation point i (which is the centre of loop i). Also, $\sigma_{\alpha\beta}^{AB\to i}$ is the $\alpha\beta$ stress of segment AB evaluated at point i. Here, the stress from all surface loops is counter-acting the stress of the subsurface dislocation segment(s) (which is given or provided as if the medium is infinite). On the right side of equation (9), although only the stress of one dislocation segment is displayed, it can instead be the sum of stresses from multiple dislocation segments (M of them) all under the free surface. Moreover, the above equations can be

rewritten as in equation (10), where each loop stress is expressed as a linear combination of the loop's Burgers vector components and 'kernel' terms which are functions of space and elastic constants. This separation of the Burgers vector components is attainable from basic linear elasticity dislocation theory (see Hirth and Lothe, 1982; Hull and Bacon, 2011). The recent work of Siddique and Khraishi (2020) has explicitly provided the kernel terms in detail based on analysis of equations (1) and (2) above provided by Devincre (1995).

$$\sum_{j=1}^{N} b_x^j K_{xxz}^{j\to i} + b_y^j K_{yxz}^{j\to i} + b_z^j K_{zxz}^{j\to i} = -\sigma_{xz}^{AB\to i}, \qquad i = 1, 2, \ldots, N \tag{10.1}$$

$$\sum_{j=1}^{N} b_x^j K_{xyz}^{j\to i} + b_y^j K_{yyz}^{j\to i} + b_z^j K_{zyz}^{j\to i} = -\sigma_{yz}^{AB\to i}, \qquad i = 1, 2, \ldots, N \tag{10.2}$$

$$\sum_{j=1}^{N} b_x^j K_{xzz}^{j\to i} + b_y^j K_{yzz}^{j\to i} + b_z^j K_{zzz}^{j\to i} = -\sigma_{zz}^{AB\to i}, \qquad i = 1, 2, \ldots, N \tag{10.3}$$

The above system represents a system of $3N$ equations, the unknowns of which are the Burgers vector components of the N loops. Once the Burgers vectors of the loops are solved for, the stress field at any material/field point P in the crystal below the surface can be calculated as follows:

$$\sigma_{\alpha\beta}^{P} = \sum_{i}^{M} \sigma_{\alpha\beta}^{i} + \sum_{j}^{N} \sigma_{\alpha\beta}^{j} \tag{11}$$

where the first sum on the right-hand side is for M dislocation segments under the surface and the second sum is for N dislocation loops meshing the free surface.

In Siddique and Khraishi (2020) paper, and in reference to Figure 9(a), the paper presented a rule of thumb based on Saint Venant's principle, to determine the accuracy of the collocation-point method for calculating stress at any given field point. The rule of thumb states that the distance (z-distance in this case) below the free surface needs to be equal or more than the average spacing between surface collocation points. For example, if each side of surface **S** in Figure 9(a) is 20,000b (where b is the Burgers vector magnitude), then if the field point is 400b below the free surface that means that the average spacing between the surface collocation points need to be at max. 400b. For the contiguous uniform mesh or grid in Figure 9(a), that means that number of elements/loops lining up each side of the surface is 50 resulting in a 50 × 50 mesh, i.e., 2,500 elements/loops minimum covering the surface.

With the advent of this paper's method/algorithm above, a different way of meshing presented in Figure 9(b) can be utilised that would cut significantly on the computation time. Figure 9(b) shows a non-uniform mesh. This mesh is called here 'on-the-fly' mesh because the idea is that one can start with a coarse (i.e., with few elements) uniform and contiguous mesh and then once a dislocation segment of a real crystal dislocation approaches the free surface in a dynamic simulation, and it is important to invoke the above-mentioned Saint Venant's rule-of-thumb, then one or more of the large surface elements could be split into smaller elements in order to get back into compliance with the rule-of-thumb. For the sake of illustration, Figure 9(b) shows that four large elements/loops in Figure 9(a) were split into four smaller elements/loops each. Notice that in this new mesh, some of the new segments for the smaller loops can intersect, in their Region 3, a collocation point in bigger loops. This will cause a numerical issue, as

pointed out above, if no proper treatment is utilised for Region 3 as introduced here in this work.

To illustrate the discussion above regarding Saint Venant's principle, on-the-fly meshing and the associated time savings when employing the collocation point method, consider a frontal view of Figures 9(a) and 9(b) in Figure 10.

Figure 10 A segment below a free surface to illustrate the principles used for meshing the surface with dislocation loops the centre of each is a collocation point (see online version for colours)

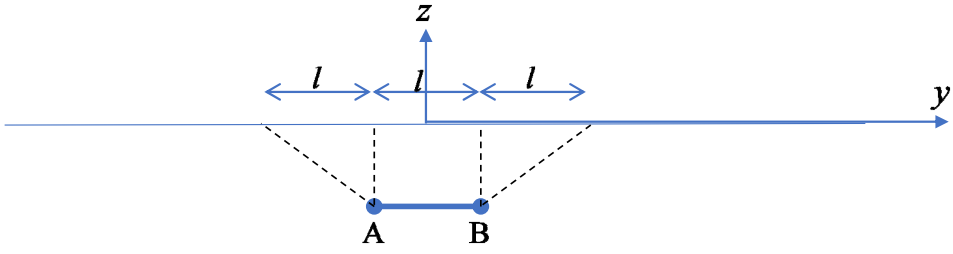

In Figure 10, a segment (called segment *AB*) is shown below a free surface. The two end points or nodes are labelled *A* and *B*. The segment is shown horizontal but could also be inclined arbitrarily. The segment, or its closest point to the surface, is at a certain depth (*z*-depth) from the surface. If as Figure 9, one considers a rectangular free surface such that each of its sides is 20,000*b* in length. Then according to Saint Venant's principle, in order for the collocation point method to work accurately it requires a spacing between the collocation points (centres of mesh elements/loops) to be equal to or less to the *z*-depth of the segment in Figure 10. Taking the *z*-depth to be 400*b*, this means that the average spacing of collocation points should be 400*b* or less. Dividing 20,000*b* by 400*b* gives 50. Therefore, the size of each of the mesh surface elements/loops in the uniform contiguous mesh in Figure 9(a) will be 400*b* or smaller. In other words, the total number of surface elements/loops is 2,500 (50 × 50 mesh) which is also the number of collocation points [*N* in equations (9) or (10)].

However, another question begs itself. When the larger elements/loops are divided into smaller ones, how big is the size of the area to be divided as such? The authors hypothesise that another/second application of Saint Venant's principle can be made here. Specifically, by looking at Figure 10, if the length of the segment is *l* (or its projected length on the free surface) then another length *l* should be added to each end of the surface projection for a total length of 3*l* (see Figure 10). Now this (3*l* × 3*l*) area can be divided into smaller elements/loops. This is the guideline to the creation of the 'on-the-fly mesh'. To test this new hypothesis, several figures/plots are created to verify it.

Figures 11, 12 and 13 show stress plots for the above-described segment *AB* which is here parallel to the free surface, by being also parallel to the *x*-axis, with the *z*-axis passing through the segment centre. However, in these plots, the field points (all parallel to the *x*-axis with $y = 0$) are at a *z*-depth = 400*b*. Specifically, the field line is from (–1,000*b*, 0, –400*b*) to (1,000*b*, 0, –400*b*). The *z*-depth for the segment in Figures 11, 12 and 13 is 1,000*b*. Also, the Burgers vector for the segment is taken as $\left(\frac{1}{\sqrt{3}}, \frac{1}{\sqrt{3}}, \frac{1}{\sqrt{3}}\right)$. In

Figures 11, 12 and 13, we first start with a coarse mesh (25 × 25 elements/loops = 625 elements/loops). Secondly, we make the first application of St. Venant's principle and thus have to use a mesh whose elements are at max 400*b* in size which generates a 50 × 50 = 2,500 loops/elements in the uniform mesh [see Figure 9(a)]. Third, we do an on-the-fly mesh by taking the centre element in the 625 mesh and dividing it into four loops/elements [similar to Figure 9(b)] to give a total of 628 loops/elements (625 – 1 + 4) in this non-uniform mesh. Fourth or lastly, we do an on-the-fly mesh by taking the centre nine elements (3 × 3) and divide each of them into four elements/loops [similar to Figure 9(b)]. This results into 652 (625 – 9 + 36) elements/loops total in this non-uniform mesh. In all of Figures 11, 12 and 13, the collocation-point method using the segment algorithm described above, was compared to a known analytical solution by Maurissen and Capella (1974a) for a parallel dislocation segment in an isotropic half medium under an infinite surface plane. To make this comparison plausible with the finite surface employed in the numerical collocation point method, the dislocation segment is placed below the centre of the surface and the surface dimensions or size is set to a large value, i.e., 20,000*b*.

Consider first Figure 11. Here, Figure 11(a) shows the 625 coarse meshes. Figure 11(b) shows the fine 2,500 elements/loops mesh. Figure 11(c) shows a non-uniform on-the-fly mesh with 628 elements, and Figure 11(d) shows a non-uniform on-the-fly mesh with 652 elements/loops. For Figure 11, we consider a segment with length $l = 100b$ [i.e., A coordinates are (–50*b*, 0, –1,000*b*) and B coordinates are (+50*b*, 0, –1,000*b*)]. For the 625 uniform meshes, the average spacing between the collocation points is 800*b*. Since the field points depth is only 400*b*, the numerical solution is not expected to (nor does it) match the analytical solution in accordance with the first application of Saint Venant's principle. This is clearly reflected in Figure 11(a). For the 2,500 mesh, the average collocation points spacing is 400*b*, so it is expected that the numerical solution matches the analytical solution for this case since the field points depth is 400*b*. Figure 11(b) shows such match. For the 628 non-uniform on-the-fly mesh, since the average collocation point spacing in the refined area right above the dislocation segment is 400*b* and the second application of Saint Venant's principle is valid (i.e., the refined mesh size of 800*b* is at least $3l = 300b$ here), it is expected to find a match between the analytical and numerical solutions. Figure 11(c) shows such match. Lastly, for the 652 non-uniform on-the-fly mesh, both applications of the Saint Venant's principle apply here and hence a match is expected between the numerical and analytical results. This is shown in Figure 11(d).

Consider Figures 12(a), 12(b), 12(c) and 12(d) which have 625 elements (uniform mesh), 2,500 elements (uniform mesh), 628 non-uniform on-the-fly mesh, and 652 non-uniform on-the-fly mesh, respectively. For Figures 12(a), 12(b), 12(c) and 12(d), we consider a segment with length $l = 200b$ [i.e., A coordinates are (–100*b*, 0, –1,000*b*) and B coordinates are (+100*b*, 0, –1,000*b*)]. Figure 12(a) does not match the analytical solution because it fails to meet the first application of Saint Venant's principle whereas Figure 12(b) does for these two uniform meshes. However, if one resorts to non-uniform meshing through on-the-fly meshing, then Figure 12(c) also shows disparity with the analytical solution since the second application of Saint Venant's fails here. However, if larger elements than one element are sub-divided into smaller ones as in the 652 mesh in Figure 12(d) then a match occurs between the analytical and numerical. This is so since the second application of Saint Venant's principle applies here. In Figure 12(d), the finer

mesh (i.e., sub-divided mesh) side length is 2,400b (3 × 800b) which is greater than 3l (600b).

Figure 11 Comparison between the numerical collocation point method solution and analytical solution of Maurissen and Capella (1974a) for a horizontal segment beneath a free surface, (a) uniform surface mesh, 625 elements (b) uniform surface mesh, 2,500 elements (c) non-uniform on-the-fly surface mesh, 628 elements (d) non-uniform on-the-fly surface mesh, 652 elements (see online version for colours)

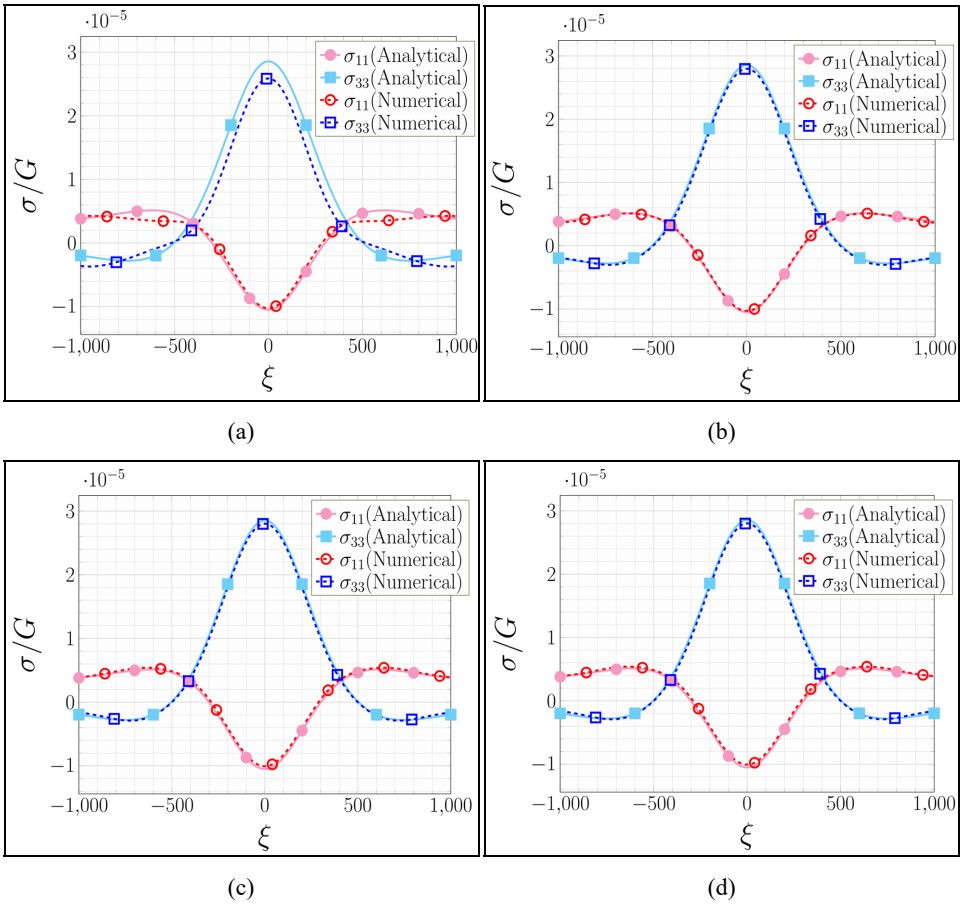

Note: Here, segment length l = 100b, i.e., A coordinates are (–50b, 0, –1,000b) and B coordinates are (+50b, 0, –1,000b).

The mismatches above with the 625 mesh and the 628 mesh continue with increased segment length l for the rest of the fixed parameters above. Now consider Figures 13(a), 13(b), 13(c) and 13(d) which also have 625 elements (uniform mesh), 2,500 elements (uniform mesh), 628 non-uniform on-the-fly mesh, and 652 non-uniform on-the-fly mesh, respectively. For Figures 13(a), 13(b), 13(c) and 13(d), we consider a segment with length l = 800b [i.e., A coordinates are (–400b, 0, –1,000b) and B coordinates are (+400b, 0, –1,000b). According to the first application of Saint Venant's principle, the 625 and 628 should not show a match between analytical and numerical solutions and Figures 13(a) and 13(c) reflect that. Also, for the 2,500 mesh there should still be a match

between the two solutions and Figure 13(b) reflect that. The small mismatch is due to the segment now being a significant percentage of the finite surface size of 20,000b which causes this situation to deviate even further from the infinite plane situation upon which the analytical solution is built. According to the second application of Saint Venant's, at this length l the 652 mesh which has a fine or sub-divided mesh equal to 3l (3 × 800b = 2,400b) should be a borderline on-the-fly mesh case for seeking a match between analytical and numerical solutions. Looking at Figure 13(d), it appears that this postulation is correct. Now if the segment length increases beyond 800b, it is expected that more mismatch will exist between the analytical and numerical solutions for the 652 mesh and that is indeed what is observed (figures are omitted here for brevity).

Figure 12 Comparison between the numerical collocation point method solution and analytical solution of Maurissen and Capella (1974a) for a horizontal segment beneath a free surface, (a) uniform surface mesh, 625 elements (b) uniform surface mesh, 2,500 elements (c) non-uniform on-the-fly surface mesh, 628 elements (d) non-uniform on-the-fly surface mesh, 652 elements (see online version for colours)

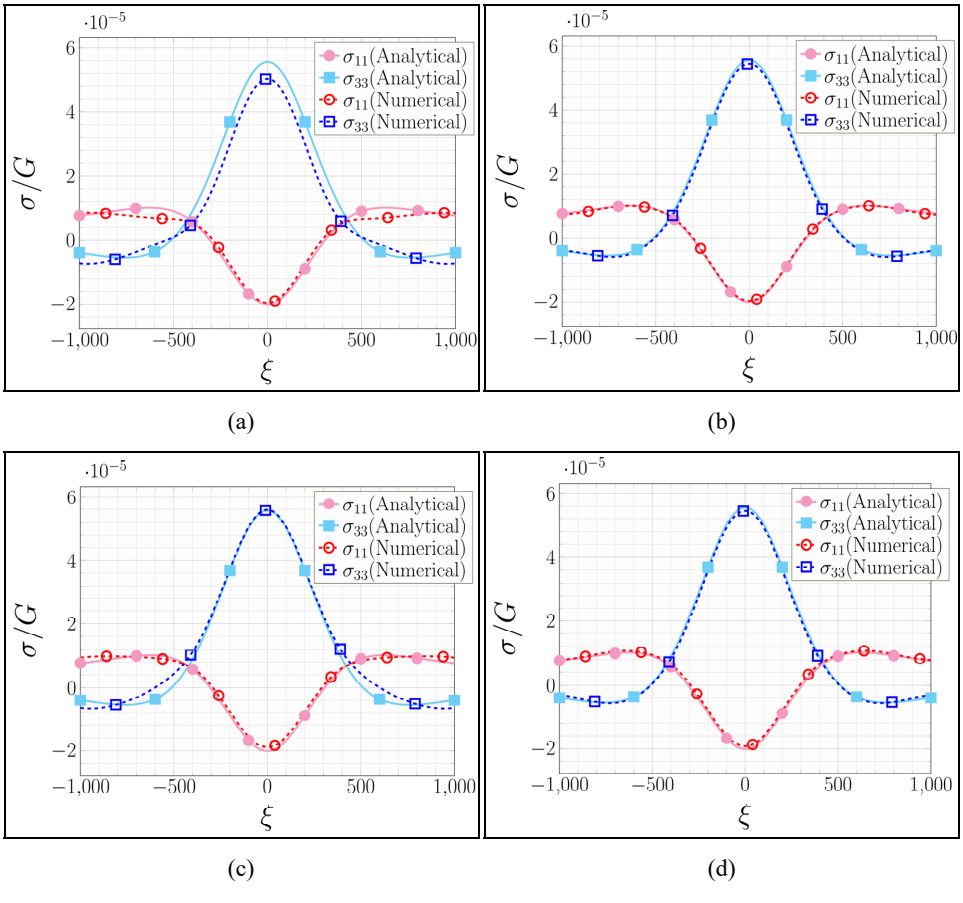

Note: Here, segment length $l = 200b$, i.e., A coordinates are (–100b, 0, –1,000b) and B coordinates are (+100b, 0, –1,000b).

Figure 13 Comparison between the numerical collocation point method solution and analytical solution of Maurissen and Capella (1974a) for a horizontal segment beneath a free surface, (a) uniform surface mesh, 625 elements (b) uniform surface mesh, 2,500 elements (c) non-uniform on-the-fly surface mesh, 628 elements (d) non-uniform on-the-fly surface mesh, 652 elements (see online version for colours)

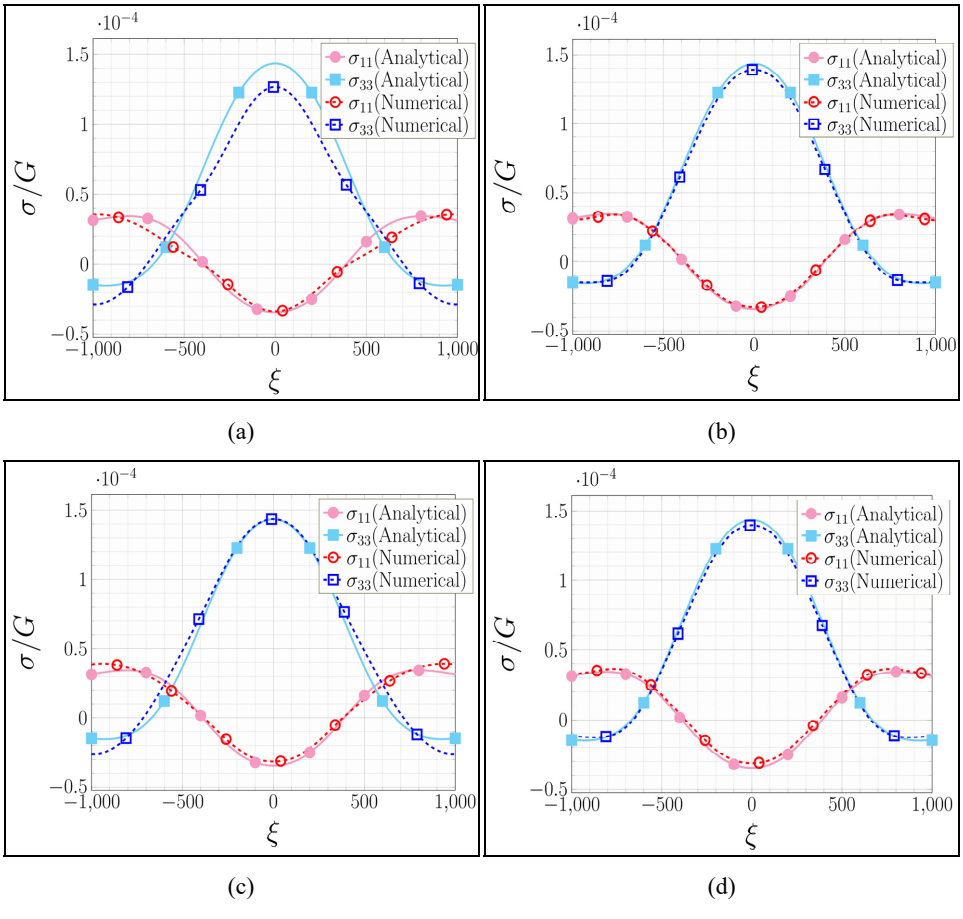

Note: Here, segment length $l = 800b$, i.e., A coordinates are ($-400b$, 0, -1,000b) and B coordinates are ($+400b$, 0, $-1{,}000b$).

The above paragraphs illustrated the first and second applications of Saint Venant's principle in as far as the collocation point numerical method is concerned. Although the first application was introduced in prior works (Khraishi et al., 2001; Khraishi and Zbib, 2002; Yan et al., 2004; Siddique and Khraishi, 2020), the second application introduced here was shown to be applicable and thus important for the on-the-fly meshing. The on-the-fly meshing was conceptualised in an effort to reduce computational time involving the system of equations (9) and (10). To show the amount of time savings in the computations, Table 2 lists the time it took to compute the stress field in Figures 11–13. Table 2 shows that for the 625, 628 and 652 the computational time is similar. However, when employing the on-the-fly meshes (i.e., 628 and 652), a great reduction in computing time occurs compared to the fine mesh used in these prior references. For example, with the 652 mesh a time reduction from the fine mesh of

91.45% which is very significant since the outputted stress results are essentially the same.

Table 2 Comparison of the computational time for on-the-fly meshes with regular uniform meshes

Number of surface elements/loops/collocation points	*Time (seconds) to compute stress field*
625	32.26
628	35.88
652	38.67
2,500	452.34

With the new segment algorithm described above, other types of meshes on a free surface (besides ones shown in Figure 9) are possible, like unstructured meshes (see Figure 14). For such meshes, especially with a high number of elements, it is possible that numerical issues stemming from the Region 3 singularity pop up when evaluating the kernel terms at collocation points representing the centre of the elements/loops (see discussion above on the collocation-point method). For this random or unstructured triangular mesh, one can plot figures similar to Figure 11–13, to show that the collocation-point method produces the correct surface correction terms ('image stresses') in compliance with Maurrisen and Capella (1974a) analytical solution. However, such plots are not provided here for brevity. For the collocation-point method described above, the term $\sigma_{xz}^{j\to i}$ in equation (9.1) becomes here equal to $\sum_{l=1}^{3}\sigma_{xz}^{jl\to i}$, where $\sigma_{xz}^{jl\to i}$ is the σ_{xz} stress component of the l^{th} segment of loop j acting at collocation point i. Similarly, for equations (9.2) and (9.3). For equation (11), $\sigma_{\alpha\beta}^{j}$ becomes for a triangular mesh with triangular loops/elements: $\sum_{l=1}^{3}\sigma_{\alpha\beta}^{jl}$, where $\sigma_{\alpha\beta}^{jl}$ is the $\sigma_{\alpha\beta}$ stress component of the l^{th} segment of loop j acting at any material/field point P.

Alternatively, one can illustrate the use of this mesh in 3D DDD simulations using the following parameters: constant strain-rate loading in the yz-direction, applied strain-rate of 10 s^{-1}, one Frank-Read source lying on the x-axis with end point coordinates of (–2,000b, 0, 0) and (2000b, 0, 0), Burgers vector $\vec{b} = (0, 1, 0)$, the computational box (or RVE) is 10,000b in each side of the cube, the shear modulus $\mu = G$ = 26.32 GPa, ν = 0.33, mass density = 2,710 kg/m^3, and the dislocation mobility equalling $1{,}000\,\frac{1}{\text{Pa}\cdot\text{s}}$. In these simulations, the unstructured triangular mesh is used on each of the six surfaces of the computational box. Figure 15 compares the stress-strain results from the DDD simulations for two situations: one not accounting for the free surface effects, and one employing the collocation point method using the mesh in Figure 14 to account for the effect of free surfaces. As can be seen in Figure 15, the incorporation of correct free surface effects reduces the flow stress in the material by about 23%. This amount is considerable and its exact number depends on factors such as the source length, the surface-to-volume ratio, etc. Additionally to above, the new algorithm can also prevent the Region 2 or Region 3 singularities from talking place when an ensemble of dislocation segments are interacting in space inside the DDD computational domain/box.

Figure 14 An unstructured triangular-element mesh used in the collocation-point method for properly treating free-surface problems in the presence of dislocations (see online version for colours)

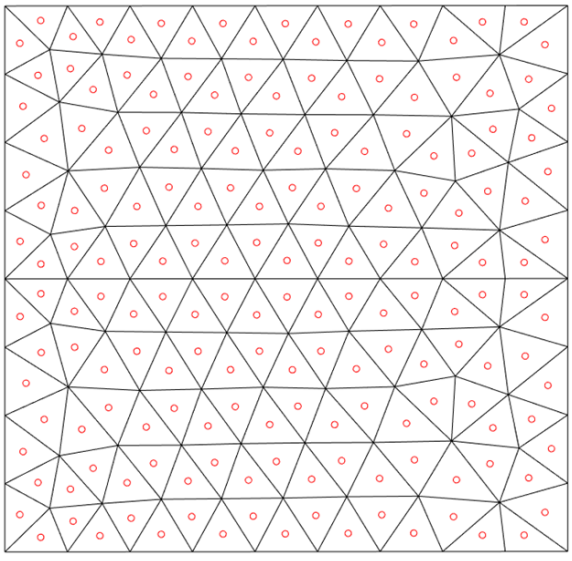

Figure 15 Stress-strain diagrams for a case with no free surface effects (no surface loops) and a case with free surface effects (triangular surface loops) (see online version for colours)

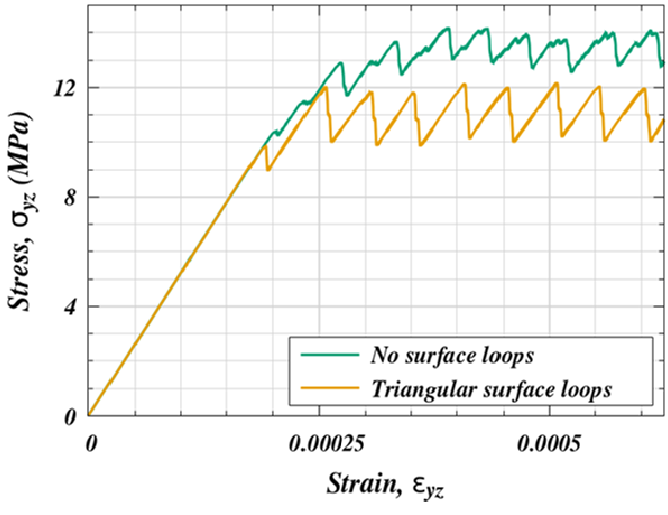

Note: The computational box is subjected to constant strain-rate loading.

Instead of using a constant-strain-rate experiment, as in Figure 15, a creep experiment can be performed. If the source is placed parallel and closely beneath a free surface, the image stresses should be enough, once overcoming the lattice friction, to pull the

dislocation out of the crystal. Figure 16 shows such simulation with the different colours showing different time shots or snaps in time. The initially straight dislocation bow outs until it gets absorbed in the surface at its middle region. The dislocation line continues to sink in the free surface until at the end only two screw segments remain on both ends.

Figure 16 A dislocation source parallel and close to a free surface (see online version for colours)

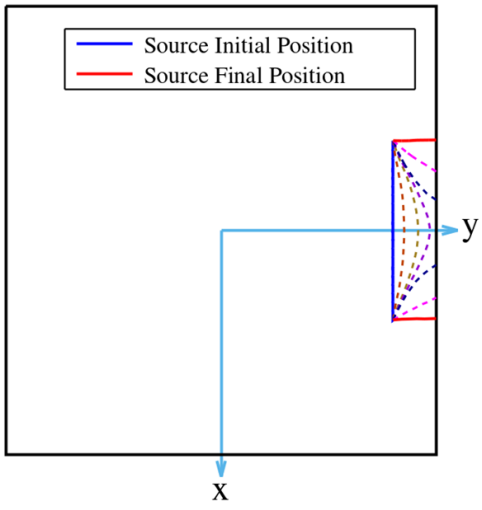

Note: The initially edge-character source gets absorbed into the free surface as shown by the time stills of the source (shown in dashed lines followed by the final source position).

4 Conclusions

Based on this research which properly treats the stress field around a dislocation segment and its trailing line, i.e., its core region, to regularise it, the following conclusions can be made. The space around the segment can be partitioned into three regions: one regular region ahead of the segment, and one with a weak singularity in the trail of the segment and one immediately around the core of the segment with a strong singularity. Also, the r_c (cut-off radius or radius of the core region) is found to be $3b$ which is a recommendation stemming out of this work. Another conclusion is that the developed algorithm expands the type of surface meshes used in collocation-point methods by allowing on-the-fly meshing or unstructured meshes. This could generate time savings in the computations. The accuracy of the meshes' results is subject to St. Venant's principle. Lastly, the research shows the importance of incorporating image-stress effects for a free surface as that could significantly impact the calculated flow stress of the material. The algorithm also could prevent problems in 3D DDD when dealing with ensembles of interacting and time-evolving dislocations in space.

References

Acharya, A. (2003) 'Driving forces and boundary conditions in continuum dislocation mechanics', *Proceedings of the Royal Society A: Mathematical, Physical and Engineering Sciences*, Vol. 459, No. 2034, pp.1343–1363, DOI: 10.1098/rspa.2002.1095.

Bacon, D.J. and Groves, P.P. (1970) 'The dislocation in a semi-infinite isotropic medium', *Fundamental Aspects of Dislocation Theory*, Vol. 1, No. 317, pp.35–45.

Baštecká, J. (1964) 'Interaction of dislocation loop with free surface', *Cechoslovackij fiziceskij zurnal B*, Vol. 14, No. 6, pp.430–442, DOI: 10.1007/BF01689476.

Cai, W., Arsenlis, A., Weinberger, C.R. and Bulatov, V.V. (2006) 'A non-singular continuum theory of dislocations', *Journal of the Mechanics and Physics of Solids*, Vol. 54, No. 3, pp.561–587, DOI: 10.1016/j.jmps.2005.09.005.

Canova, G.R. and Fivel, M.C. (1999) 'Developing rigorous boundary conditions to simulations of discrete dislocation dynamics', *Modelling and Simulation in Materials Science and Engineering*, Vol. 7, No. 5, pp.753–768.

Chou, Y.T. (1963) 'The energy of circular dislocation loops in thin plates', *Acta Metallurgica*, Vol. 11, No. 8, pp.829–834, DOI: 10.1016/0001-6160(63)90051-8.

Comninou, M. and Dundurs, J. (1975) 'The angular dislocation in a half space', *Journal of Elasticity*, Vol. 5, Nos. 3–4, pp.203–216, DOI: 10.1007/BF00126985.

de Wit, R. (1967) 'Some relations for straight dislocations', *Physica Status Solidi (B)*, Vol. 20, No. 2, pp.567–573, DOI: 10.1002/pssb.19670200217.

Demir, I. and Khraishi, T.A. (2005) 'The torsional dislocation loop and mode III cylindrical crack', *Journal of Mechanics*, Vol. 21, No. 2, pp.109–116, DOI: 10.1017/S1727719100004585.

Deng, J., El-Azab, A. and Larson, B.C. (2008) 'On the elastic boundary value problem of dislocations in bounded crystals', *Philosophical Magazine*, Vol. 88, Nos. 30–32, pp.3527–3548, DOI: 10.1080/14786430802558544.

Devincre, B. (1995) 'Three dimensional stress field expressions for straight dislocation segments', *Solid State Communications*, Vol. 93, No. 11, pp.875–878.

Devincre, B., Hoc, T. and Kubin, L.P. (2008) 'Dislocation mean free paths and strain hardening of crystals', *Science*, Vol. 320, No. 5884, pp.1745–1748, DOI: 10.1126/science.1156101.

El-Azab, A. (2000) 'The boundary value problem of dislocation dynamics', *Modelling and Simulation in Materials Science and Engineering*, Vol. 8, No. 1, pp.37–54.

Ghoniem, N. and Sun, L.Z. (1999) 'Fast-sum method for the elastic field of three-dimensional dislocation ensembles', *Physical Review B – Condensed Matter and Materials Physics*, Vol. 60, No. 1, pp.128–140, DOI: 10.1103/PhysRevB.60.128.

Groves, P.P. and Bacon, D.J. (1970) 'The dislocation loop near a free surface', *Philosophical Magazine*, Vol. 22, No. 175, pp.83–91, DOI: 10.1080/14786437008228153.

Hartmaier, A., Fivel, M.C., Canova, G.R. and Gumbsch, P. (1999) 'Image stresses in a free-standing thin film', *Modelling and Simulation in Materials Science and Engineering*, Vol. 7, No. 5, pp.781–793, DOI: 10.1088/0965-0393/7/5/310.

Hills, D.A., Kelly, P.A., Dai, D.N. and Korsunsky, A.M. (1996) *Solution of Crack Problems: The Distributed Dislocation Technique*, Springer, Dordrecht, The Netherlands.

Hirth, J.P. and Lothe, J. (1982) *Theory of Dislocations*, 2nd ed., Krieger Publishing Company, Malabar, Florida.

Hull, D. and Bacon, D.J. (2011) *Introduction to Dislocations*, 5th ed., Butterworth-Heinemann, New York.

Jamond, O., Gatti, R., Roos, A. and Devincre, B. (2016) 'Consistent formulation for the discrete-continuous model: improving complex dislocation dynamics simulations', *International Journal of Plasticity*, Vol. 80, pp.19–37, DOI: 10.1016/j.ijplas.2015.12.011.

Jing, P., Khraishi, T.A., Ruiz, L.A.Z. and Wirth, B.D. (2009) 'The elastic fields of sub-surface dislocation loops: a comparison between analytical continuum-theory solutions and atomistic calculations', *International Journal of Theoretical and Applied Multiscale Mechanics*, Vol. 1, No. 1, pp.71–85, DOI: 10.1504/ijtamm.2009.022472.

Khraishi, T.A. and Demir, I. (2003) 'On Cauchy singular integrals and stress intensity factors for 2D mode I cracks in an infinite solid', *Mechanics Research Communications*, Vol. 30, No. 4, pp.353–364, DOI: 10.1016/S0093-6413(03)00032-6.

Khraishi, T.A. and Shen, Y-L. (2011) *Introductory Continuum Mechanics with Applications to Elasticity. Revised*, University Readers/Cognella, San Diego, California.

Khraishi, T.A. and Zbib, H.M. (2001) 'Dislocation dynamics simulations of the interaction between a short rigid fiber and a glide circular dislocation pile-up', *Computational Materials Science*, Vol. 24, pp.310–322, DOI: 10.1016/S0927-0256(01)00253-1.

Khraishi, T.A. and Zbib, H.M. (2002) 'Free-surface effects in 3D dislocation dynamics: formulation and modeling', *Journal of Engineering Materials and Technology*, Vol. 124, No. 3, pp.342–351, DOI: 10.1115/1.1479694.

Khraishi, T.A., Yan, L. and Shen, Y-L. (2004) 'Dynamic simulations of the interaction between dislocations and dilute particle concentrations in metal-matrix composites (MMCs)', *International Journal of Plasticity*, Vol. 20, No. 6, pp.1039–1057, DOI: 10.1016/j.ijplas. 2003.10.003.

Khraishi, T.A., Zbib, H.M. and De La Rubia, T.D. (2001) 'The treatment of traction-free boundary condition in three-dimensional dislocation dynamic using generalized image stress analysis', *Materials Science and Engineering A*, Vols. 309–310, pp.283–287, DOI: 10.1016/S0921-5093(00)01727-5.

Kubin, L.P., Canova, G.R., Condat, M., Devincre, B., Pontikis, V. and Bréchet, Y. (1992) 'Dislocation microstructures and plastic flow: a 3D simulation', *Solid State Phenomena*, Vols. 23–24, pp.455–472, DOI: 10.4028/www.scientific.net/ssp.23-24.455.

Leger, R.W., Khraishi, T.A. and Shen, Y.L. (2004) 'A dislocation dynamics study of strength differential in particle-containing metals during cyclic loading', *Journal of Materials Science*, Vol. 39, No. 11, pp.3593–3604, DOI: 10.1023/B:JMSC.0000030711.66044.92.

Li, L. and Khraishi, T.A. (2021) 'Strain field development of a rectangular dislocation loop in a semi-infinite medium with verification', *Physical Science International Journal*, Vol. 25, No. 1, pp.23–38, DOI: 10.9734/psij/2021/v25i130234.

Li, L., Khraishi, T.A. and Siddique, A.B. (2021) 'The strain/stress fields of a subsurface rectangular dislocation loop parallel to the surface of a half medium: analytical solution with verification', *Journal of Applied Mathematics and Physics*, Vol. 9, No. 1, pp.146–175, DOI: 10.4236/jamp. 2021.91011.

Lothe, J., Indenbom, V.L. and Chamrov, V.A. (1982) 'Elastic field and self-force of dislocations emerging at the free surfaces of an anisotropic halfspace', *Physica Status Solidi (B)*, Vol. 111, No. 2, pp.671–677, DOI: 10.1002/pssb.2221110231.

Maurissen, Y. and Capella, L. (1974a) 'Stress field of a dislocation segment parallel to a free surface', *Philosophical Magazine*, Vol. 29, No. 5, pp.1227–1229, DOI: 10.1080/ 14786437408226608.

Maurissen, Y. and Capella, L. (1974b) 'Stress field of a dislocation segment perpendicular to a free surface', *Philosophical Magazine*, Vol. 30, No. 3, pp.679–683, DOI: 10.1080/ 14786439808206591.

Meyers, M.A. and Chawla, K.K. (2009) *Mechanical Behavior of Materials*, 2nd ed., Cambridge University Press, Cambridge, UK.

Schulz, K., Dickel, D., Schmitt, S., Sandfeld, S., Weygand, D. and Gumbsch, P. (2014) 'Analysis of dislocation pile-ups using a dislocation-based continuum theory', *Modelling and Simulation in Materials Science and Engineering*, Vol. 22, No. 2, pp.1–15, DOI: 10.1088/0965-0393/ 22/2/025008.

Siddique, A.B. and Khraishi, T.A. (2020) 'Numerical methodology for treating static and dynamic dislocation problems near a free surface', *Journal of Physics Communications*, Vol. 4, No. 5, DOI: 10.1088/2399-6528/ab8ff9.

Siddique, A.B. and Khraishi, T.A. (2021a) 'A mesh-independent brute-force approach for traction-free corrections in dislocation problems', *Modeling and Numerical Simulation of Material Science*, Vol. 11, No. 1, pp.1–18, DOI: 10.4236/mnsms.2021.111001.

Siddique, A.B. and Khraishi, T.A. (2021b) 'Screw dislocations around voids of any shape: a generalized numerical approach', *Forces in Mechanics*, October 2020, Vol. 3, p.100014, DOI: 10.1016/j.finmec.2021.100014.

Weeterman, J. and Weeterman, J.R. (1992) *Elementary Dislocation Theory*, Oxford University Press, Oxford.

Yan, L., Khraishi, T.A., Shen, Y-L. and Horstemeyer, M.F. (2004) 'A distributed-dislocation method for treating free-surface image stresses in three-dimensional dislocation dynamics simulations', *Modelling and Simulation in Materials Science and Engineering*, Vol. 12, No. 4, DOI: 10.1088/0965-0393/12/4/S01.

Yoffe, E.H. (1961) 'A dislocation at a free surface', *Philosophical Magazine*, Vol. 6, No. 69, pp.1147–1155, DOI: 10.1080/14786436108239675.

Zbib, H.M., Rhee, M. and Hirth, J.P. (1998) 'On plastic deformation and the dynamics of 3D dislocations', *International Journal of Mechanical Sciences*, Vol. 40, Nos. 2–3, pp.113–127, DOI: 10.1016/S0020-7403(97)00043-X.

Zhu, Y. and Xiang, Y. (2015) 'A continuum model for dislocation dynamics in three dimensions using the dislocation density potential functions and its application to micro-pillars', *Journal of the Mechanics and Physics of Solids*, Vol. 84, pp.230–253, DOI: 10.1016/j.jmps.2015.07.015.